Characterizing Scalar Metasurfaces Using Time-Domain Reflectometry

TOMÁŠ DOLEŽAL[ID], **(Student Member, IEEE), PETR KADLEC**[ID], **(Member, IEEE), AND MARTIN ŠTUMPF**[ID], **(Senior Member, IEEE)**

Lerch Laboratory of EM Research, Department of Radioelectronics, Faculty of Electrical Engineering and Communication, Brno University of Technology, 60190 Brno, Czech Republic

Corresponding author: Martin Štumpf (martin.stumpf@centrum.cz)

ABSTRACT Two efficient methodologies for the determination of electromagnetic (EM) constitutive properties of scalar metasurfaces are introduced and discussed. In contrast to the available methods, and in line with the recent increasing interest in time-domain (TD) analyses of metasurfaces, we show that the material parameters of a scalar metasurface can be readily achieved directly in the TD merely from the EM reflected pulse shape. The two methodologies are based on an analytical TD reflectometry (TDR) approach and a modern stochastic optimization technique. A number of illustrative numerical examples demonstrating the validity and properties of the proposed techniques are presented.

INDEX TERMS Electromagnetic transient scattering, inverse scattering problem, metasurface, time-domain analysis.

I. INTRODUCTION

Time-domain (TD) reflectometry (TDR) is an efficient non-destructive testing methodology that is based on the detection and subsequent interpretation of a pulsed electromagnetic (EM) field signal reflected by a device under test [1]. It has found a wealth of applications in remote characterization of faulty electric transmission-line systems [2], ultra-wide-band antennas [3], radar targets [4], optical fibers [5] and many others. The present paper aims at proposing new applications of TDR to the determination of EM constitutive properties of a class of metasurfaces.

Generally, metasurfaces can be viewed as purposefully created thin screens that hold great promise for designing novel high-performance antennas, absorbers [6] and lenses [7] (see [8], for other relevant references). Their design can be based on analytical models (e.g. [9]), or more generally, on dedicated numerical techniques (see [10]–[13], for example) that incorporate cross-layer transition conditions [14], [15]. The latter approach has been recently pursued in Ref. [16], where the conjugate gradient minimization is applied to achieve the desired source distributions. While being robust and efficient, this

---

The associate editor coordinating the review of this manuscript and approving it for publication was Giovanni Angiulli[ID].

approach is limited to harmonic fields, and thus to linear and time-invariant metasurfaces. The same limitation applies to Refs. [17], [18], where the frequency-domain (FD) method of moments is applied to synthesize metasurface holograms.

In order to exploit application potentialities offered by space-time metamaterials [19], [20], both direct and inverse modeling procedures have to be formulated in the TD [21]. An initial contribution to this effort is presented in this article, where we introduce two efficient methodologies capable of extracting material properties of a scalar metasurface from the pulse reflected by the metasurface. The first TDR approach is analytic and is inspired by the TDR experiment designed for the detection, localization and characterization of faults in power lines [22]. The second methodology relies on a stochastic optimization approach, the feasibility of which has been demonstated in [23]. The (forward) mathematical model employed in both inversion approaches is based on the TD saltus-type conditions applying to thin screens with combined magneto-dielectric properties [15].

II. PROBLEM DEFINITION

The problem under consideration is shown in Fig. 1. Position in the examined configuration in the 3-D space $\mathbb{R}^3$ is specified by coordinates $\{x, y, z\}$ with respect to an orthogonal Cartesian coordinate system with the origin $\mathcal{O}$
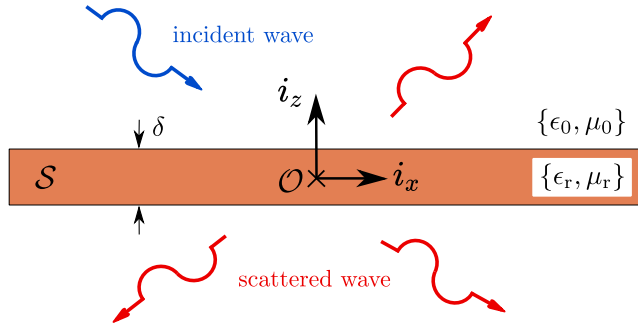
FIGURE 1. The examined scalar metasurface embedded in a homogenous, isotropic and loss-free background medium.

and unit vectors $\{i_x, i_y, i_z\}$ forming the standard base. We shall analyze the pulsed EM field scattered by the metasurface, which is located in a homogenous isotropic and loss-free medium described by the electric permittivity ϵ_0 and magnetic permeability μ_0. We assume that the layer occupies $\mathcal{S} = \{(x, y) \in \Sigma, -\delta/2 < z < \delta/2\} \subset \mathbb{R}^3$, where $\Sigma \subset \mathbb{R}^2$ is the surface of the layer in the xy plane and δ its thickness.

It is noted that the electric permittivity and magnetic permeability in the real-frequency domain may have an imaginary part. The present analysis, however, is carried out entirely in the TD, where losses manifest themselves through additional time-convolution operators in the EM constitutive relations.

Metasurfaces are frequently designed by arranging a relatively large number of small scatterers into a 2-D regular pattern of vanishing thickness. To simplify the modeling of their complex structure, the EM scattering by such surfaces is commonly analyzed using bulk material parameters. This model, in line with the broad definition given in Ref. [20], is also adopted in the present work. In particular, for the sake of simplicity, the metasurface is assumed to be described by the (homogenized) relative electric permittivity and relative magnetic permeability, which are the desired material parameters to be extracted. The (mostly negligible) effect of electric conductivity or/and linear magnetic hysteresis losses can be incorporated through the model introduced in Ref. [15].

III. SOLUTION METHODOLOGIES

In this section we shall describe two approaches to achieving the relative electric permittivity ϵ_r and relative magnetic permeability μ_r of the scalar metasurface (see Fig. 1). The employed scattering model relies heavily on the results introduced in [15].

A. ANALYTICAL APPROACH

The inverse material characterization methodology described in this section is based on the idea hinted at in [22] regarding a TD reflectometric scheme for characterizing faults on a transmission line. Combining the ideas presented in Refs. [15] and [22], the desired material parameters can be precisely determined with minimal computational complexity.

Without any loss of generality we assume that the examined layer is irradiated by an impulsive y-independent, TE-polarized EM plane-wave defined as:

$$E_y^i(x, z, t) = e^i(t - p_0 x + \gamma_0 z) \tag{1}$$

where $p_0 = \sin(\beta)/c_0$ and $\gamma_0 = \cos(\beta)/c_0$ are the slowness parameters in the x and z direction, β is the angle of incidence and c_0 is the corresponding EM wave speed. The TD wave reflected from the scalar metasurface represented by [15, Eq. (10)] can be with the aid of the Laplace transform written as

$$\hat{E}_y^r(x, z, s) = e^i(s) \left[\frac{\Psi}{s + \Psi} - \frac{\Omega}{s + \Omega} \right] \exp\left[-s(p_0 x + \gamma_0 z)\right] \tag{2}$$

where s is the Laplace-transform parameter ($=$ complex frequency). Furthermore, Ψ and Ω represent the influence of the desired parameters ϵ_r and μ_r via [15, Eqs. (11, 12)]

$$\Psi = \frac{2Y_0 \cos(\beta)}{\delta \epsilon_0 \epsilon_r} \tag{3}$$

$$\Omega = \frac{2}{Y_0 \cos(\beta) \delta \mu_0 \mu_r} \tag{4}$$

where $Y_0 = \sqrt{\epsilon_0/\mu_0}$ denotes the wave admittance and δ is the thickness of the layer. Adopting further the TDR methodology presented in Ref. [22], the plane-wave signature of the incident EM field is described by the exponential pulse:

$$e^i(t|\alpha) = e_m \exp(-\alpha t) H(t) \tag{5}$$

where e_m is the pulse amplitude and α denotes the pulse decay coefficient. It is noted that the decay coefficient corresponds to $1/t_w$, where t_w is the pulse time width. The s-domain counterpart of Eq. (5) then immediately follows as

$$\hat{e}^i(s|\alpha) = \frac{e_m}{s + \alpha} \tag{6}$$

Combining Eq. (2) with (6), transforming the result to the TD, we find at once

$$\begin{aligned} E_y^r(x, z, t'|\alpha) = {} & \frac{e_m \Psi}{\Psi - \alpha} \left[\exp(-\alpha t') - \exp(-\Psi t')\right] H(t') \\ & - \frac{e_m \Omega}{\Omega - \alpha} \left[\exp(-\alpha t') - \exp(-\Omega t')\right] H(t') \end{aligned} \tag{7}$$

where $t' = t - p_0 x - \gamma_0 z$ and $H(t)$ denotes the Heaviside unit-step function.

1) CALCULATION PROCEDURE

The closed-form TD expression (7) specifying the pulse reflected against a scalar metasurface will be next used to determine its constitutive material properties. To that end, we shall conduct two experiments considering two distinct exponential-pulse excitations that differ in their pulse decay coefficients. For the sake of clarity, we denote these experiments and its corresponding α-coefficients as follows

$$\text{Experiment A} \rightarrow \alpha = \alpha_A \tag{8}$$

$$\text{Experiment B} \rightarrow \alpha = \alpha_B \tag{9}$$

Consequently, Eq. (5) can be used to represent the two pulses in experiments A and B as $e^i(t|\alpha_{A,B}) = e_m \exp(-\alpha_{A,B}t)H(t)$. Upon carrying out these experiments, we get two reflected pulses from which we can extract their peaks and the corresponding instants.

The first step is to calculate the echograms $E_y^r(x, z, t'|\alpha_A)$ for experiment A and $E_y^r(x, z, t'|\alpha_B)$ for experiment B. For the sake of brevity, we shall further drop the (unit) amplitudes of the incident pulses and consider the normalized reflected fields $E_y^r(x, z, t'|\alpha_A)/e_m$, $E_y^r(x, z, t'|\alpha_B)/e_m$.

Consequently, using Eq. (7) we obtain

$$
E_y^r(x, z, t'|\alpha_{A,B})
$$
$$
= \frac{\Psi}{\Psi - \alpha_{A,B}} \left[\exp(-\alpha_{A,B}t') - \exp(-\Psi t') \right] H(t')
$$
$$
- \frac{\Omega}{\Omega - \alpha_{A,B}} \left[\exp(-\alpha_{A,B}t') - \exp(-\Omega t') \right] H(t') \quad (10)
$$

Next, taking the time differentiation of Eq. (10) we find instants $t_{r;\alpha_A}$ and $t_{r;\alpha_B}$ at which $\partial_t E_y^r(x, z, t'|\alpha_A) = 0$ and $\partial_t E_y^r(x, z, t'|\alpha_B) = 0$, respectively. Pursuing this approach, we end up with the following (independent) equations

$$
\partial_t E_y^r(x, z, t'|\alpha_{A,B})
$$
$$
= \left[\frac{\Psi^2 \exp(-\Psi t') - \alpha_{A,B}\Psi \exp(-\alpha_{A,B}t')}{\Psi - \alpha_{A,B}} \right.
$$
$$
\left. - \frac{\Omega^2 \exp(-\Omega t') - \alpha_{A,B}\Omega \exp(-\alpha_{A,B}t')}{\Omega - \alpha_{A,B}} \right] H(t') = 0
$$
$$
(11)
$$

In practice, the time derivative is calculated using a suitable finite-difference approximation.

2) ILLUSTRATIVE EXAMPLE

In the following example, the probed metasurface is excited by the uniform plane waves with the unit amplitudes $e_m = 1\,\text{V/m}$ with the angle of incidence $\beta = \pi/4$ rad. The interrogation pulses, shown in Fig. 2, are further described by their decay coefficients $\alpha_A = 1\,\text{ps}^{-1}$ and $\alpha_B = 0.5\,\text{ps}^{-1}$. For this instance, the layer under consideration is characterized by thickness $\delta = 50\,\mu\text{m}$ and $\epsilon_r = 18$, $\mu_r = 6$.

Figure 3 represents Eq. (10) for the selected parameters of the incident pulses and metasurface. Figure 4 shows a graphical representation of the solutions of Eq. (11) for the selected parameters of the incident pulses and the metasurface. The corresponding peaks, indicated in Fig. 3, are denoted by $E_{p;\alpha_A} = E_y^r(x, z, t_{r;\alpha_A}|\alpha_A)$, $E_{p;\alpha_B} = E_y^r(x, z, t_{r;\alpha_B}|\alpha_B)$.

Substituting the data extracted from the echograms, $(t_{r;\alpha_{A,B}}, E_{p;\alpha_{A,B}})$, in Eq. (10), we end up with a system of two (non-linear) Eqs. (12a), (12b) with two unknowns Ψ and Ω. Its solution finally yields via Eqs. (3) and (4) the desired material parameters ϵ_r and μ_r.

$$
E_{p;\alpha_A} = \frac{\Psi}{\Psi - \alpha_A} \left[\exp(-\alpha_A t_{r;\alpha_A}) - \exp(-\Psi t_{r;\alpha_A}) \right]
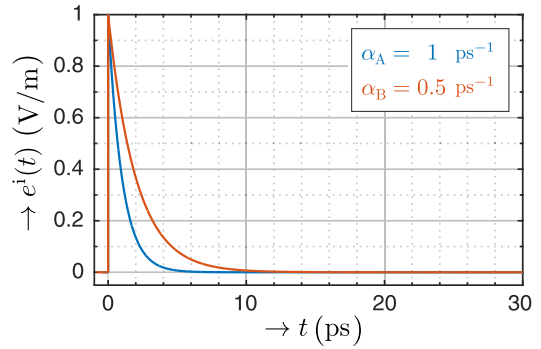$$

FIGURE 2. Exponential incident pulse shape $e^i(t|\alpha_A)$ and $e^i(t|\alpha_B)$.
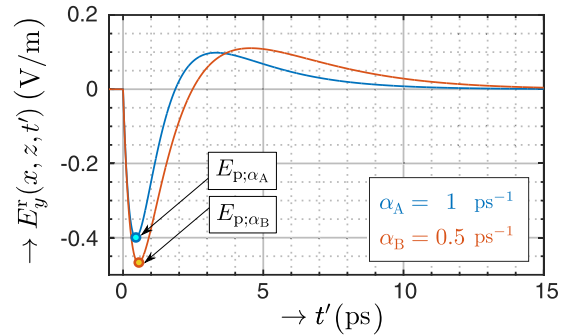

FIGURE 3. Calculated echo waveforms $E_y^r(x, z, t'|\alpha_A)$ and $E_y^r(x, z, t'|\alpha_B)$.
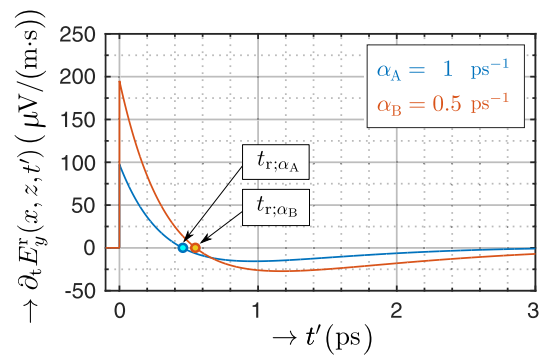

FIGURE 4. Time differentiation of echo waveforms $\partial_t E_y^r(x, z, t'|\alpha_A)$ and $\partial_t E_y^r(x, z, t'|\alpha_B)$.

$$
- \frac{\Omega}{\Omega - \alpha_A} \left[\exp(-\alpha_A t_{r;\alpha_A}) - \exp(-\Omega t_{r;\alpha_A}) \right] \quad (12a)
$$
$$
E_{p;\alpha_B} = \frac{\Psi}{\Psi - \alpha_B} \left[\exp(-\alpha_B t_{r;\alpha_B}) - \exp(-\Psi t_{r;\alpha_B}) \right]
$$
$$
- \frac{\Omega}{\Omega - \alpha_B} \left[\exp(-\alpha_B t_{r;\alpha_B}) - \exp(-\Omega t_{r;\alpha_B}) \right] \quad (12b)
$$

### B. GLOBAL OPTIMIZATION APPROACH

A method for characterization of thin–sheet metasurfaces was introduced in [23]. The method is based on the cooperation of an arbitrary stochastic optimizer with a relatively new model to the TD EM fields in the vicinity of a metasurface with combined magneto-dielectric properties. This TD solution is used as the forward solver that evaluates the candidate

TABLE 1. Controlling parameters of the PSO algorithm as recommended in [29].

Parameter	Symbol	Value (−)
Number of agents	N^{A}	100
Number of iterations	N^{I}	100
Inertia weight	w	$[0.9, \ldots, 0.4]$
Cognitive learning factor	c_1	1.5
Social learning factor	c_2	1.5
Boundary type	BT	reflecting
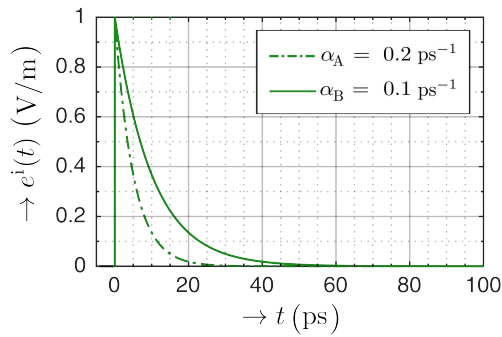
(a) The first pair of pulses
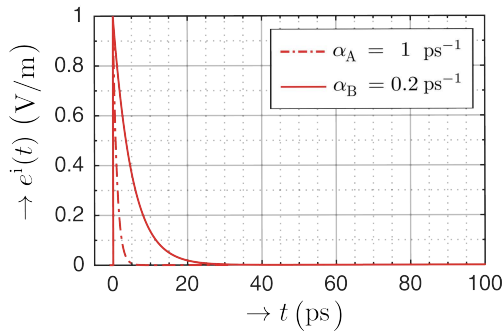
(b) The second pair of pulses

FIGURE 5. Two distinct pairs of exponential excitation pulses.

TABLE 2. Case 1 – Selected values of $\alpha_{\mathrm{A,B}}$, β and δ. ($\epsilon_r = 50$, $\mu_r = 3$, $\delta = 10\ \mu$m).

β (rad)	α_{A} (ps^{-1})	α_{B} (ps^{-1})
$\pi/4$	0.2	0.1
	1.0	0.2
$3\pi/40$	0.2	0.1
	1.0	0.2

solutions $\boldsymbol{u}$ proposed by the global optimization algorithm that solves the single-objective optimization problem that can be formulated as follows:

$$\min_{\boldsymbol{u}} f(\boldsymbol{u}) = \frac{1}{N}\sum_{n=1}^{N}[E_n^{\mathrm{comp}}(\boldsymbol{r}, \boldsymbol{u}) - E_n^{\mathrm{true}}(\boldsymbol{r})]^2$$

$$\text{s.t. } \boldsymbol{u} \in \Gamma \tag{13}$$

TABLE 3. Case 2 – Selected values of $\alpha_{\mathrm{A,B}}$, β and δ. ($\epsilon_r = 50$, $\mu_r = 3$, $\beta = \pi/4$ rad).

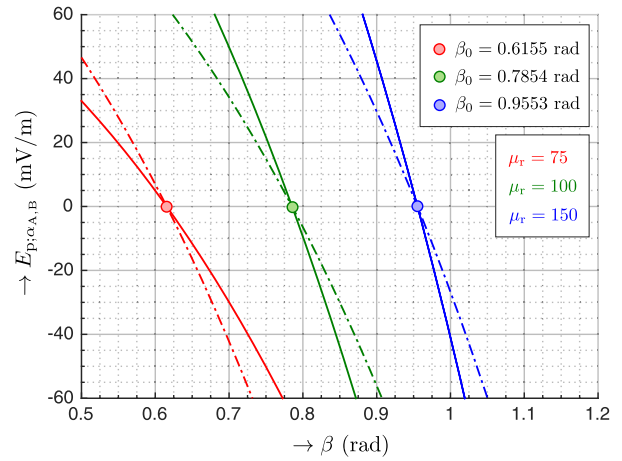| δ (μm)	α_{A} (ps^{-1})	α_{B} (ps^{-1})
5	0.2	0.1
	1.0	0.2
15	0.2	0.1
	1.0	0.2

FIGURE 6. Graphical demonstration of the angles of incidence β_0 for three different values $\mu_r = \{75; 100; 150\}$ and constant $\epsilon_r = 50$, $\alpha_{\mathrm{A}} = 1$ ps^{-1} (solid line), $\alpha_{\mathrm{B}} = 0.2$ ps^{-1} (dash-and-dot line).

Here, N is the total number of discrete time samples n, $\boldsymbol{r}$ is the position vector where the electric field is observed. Symbols E^{comp} and E^{true} denote the "computed (optimized)" and "true (measured)" observed electric field, respectively. Candidate solutions $\boldsymbol{u}$ are vectors $\boldsymbol{u} = \{\epsilon_r, \mu_r\}$ that can be located at the decision space Γ.

Generally, the optimization problem defined by (13) can be solved by any single-objective optimization. However, the comparative study [23] proved that Particle Swarm Optimization (PSO) algorithm [24] can solve that problem in the most effective way from the set of algorithms containing four other state-of-the-art algorithms namely: Genetic Algorithm [25], Differential Evolution [26], Invasive Weed Optimization [27], and Covariance Matrix Adaptation–Evolutionary Strategy [28]. Therefore, only the PSO algorithm is used in this study.

PSO is a representative of the so-called swarm intelligence algorithms. The set of particles (decision space vectors $\boldsymbol{u}$) co-operates to search for the position with the best value of the objective function. All the particles move in the decision space with a different velocity. The velocity of every particle is updated based on a combination of three procedures: 1) the particle is forced to continue in the random inertial movement, 2) the particle is attracted to its personal best position (position visited by the particle with the so-far best value of the objective function), and 3) the particle is attracted
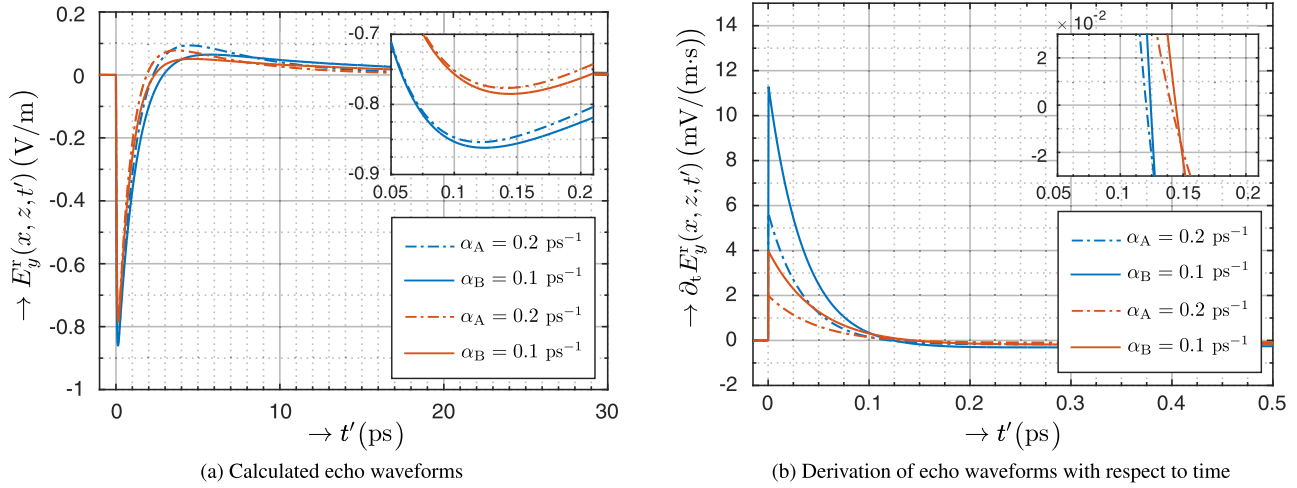
(a) Calculated echo waveforms

(b) Derivation of echo waveforms with respect to time

FIGURE 7. Case 1 – Reflected pulse shapes and its time derivative for the first pair of excitation pulses ($\beta = 3\pi/40$ rad – orange, $\beta = \pi/4$ rad – blue).

(a) Calculated echo waveforms
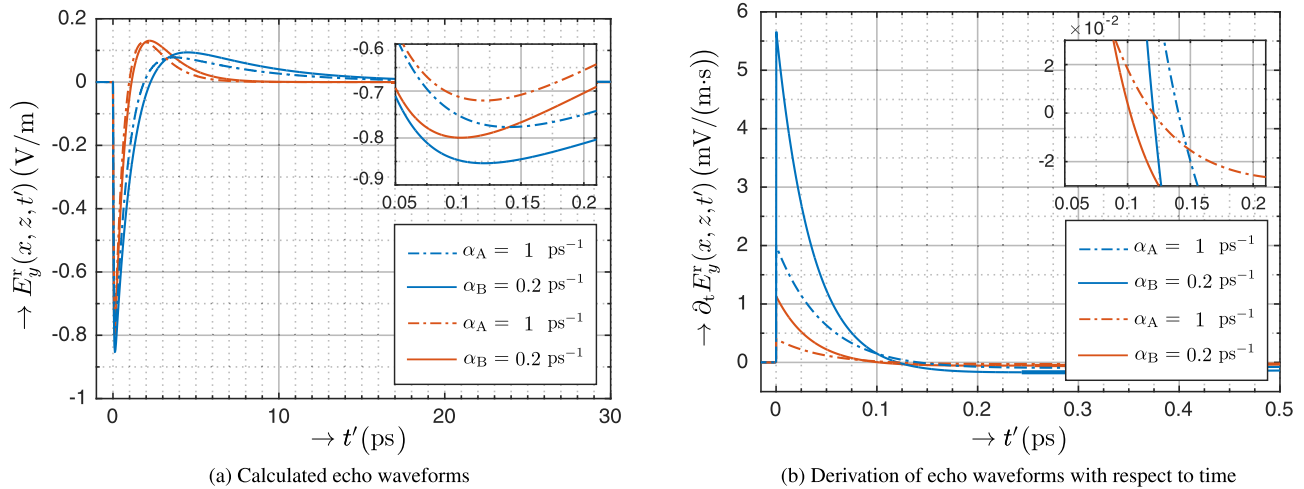
(b) Derivation of echo waveforms with respect to time

FIGURE 8. Case 1 – Reflected pulse shapes and its time derivative for the second pair of excitation pulses ($\beta = 3\pi/40$ rad – orange, $\beta = \pi/4$ rad – blue).

to the global best position (the best position from all personal best positions in the swarm). Therefore, the particle uses cognitive learning (it benefits from its own experience) and social learning (it benefits from the knowledge of the whole swarm) as well. The balance between the exploration and exploitation of the algorithm is made by the balance of weights for the individual procedures 1-3. For more details about the principles of PSO, the reader is refered to [24]. The MATLAB implementation of the PSO algorithm in the software package FOPS [29] is used in this study.

The trade–off between all three ''forces'' mentioned above can be set by user-defined controlling parameters. The inertia weight w forces particles to explore the decision space Γ, the cognitive learning factor c_1 supports the local exploitation of the area near the personal best, and the social learning factor c_2 favors the exploitation of the area near the global bets.

All the controlling parameters of the PSO algorithm used in this study are summarized in Tab. 1.

All the results presented below are based on statistical data collected for 100 repetitions of every optimization run.

IV. NUMERICAL EXAMPLES

A. ANALYTICAL APPROACH

In this subsection, we present the results of the analytical approach for a variety of selected parameters β (= the angle of incidence) or δ (= the layer's thickness). Furthermore, we will perform the calculation for two distinct pairs of interrogation pulses illustrated in Fig. 5. Thus, both experiments A and B will be carried out twice (see Eqs. (8) and (9)).

For the analytical model to apply, the metasurface is assumed to be very thin with respect to the spatial support of
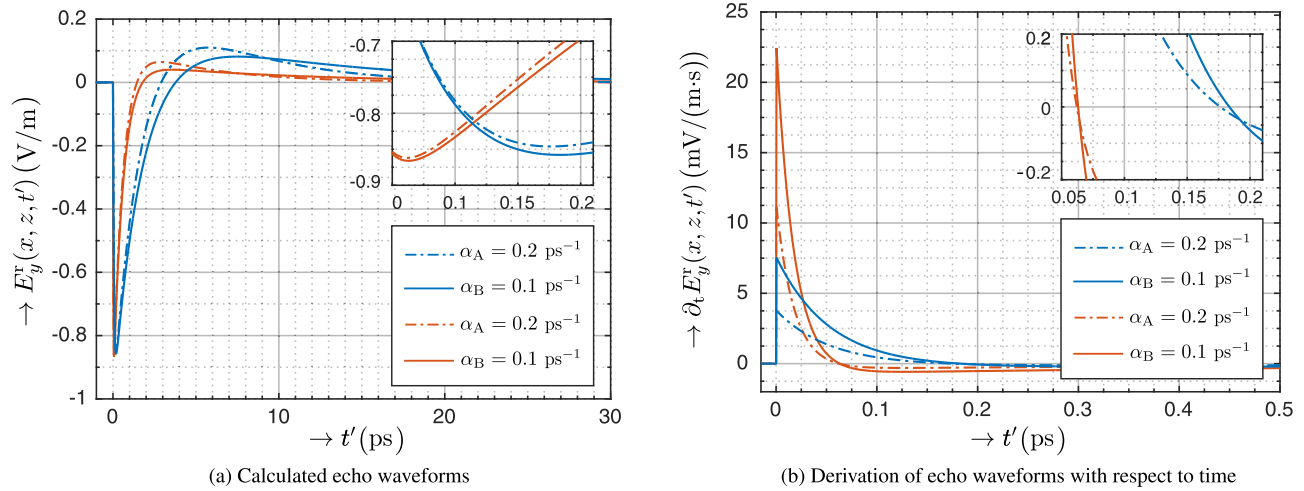
FIGURE 9. Case 2 – Reflected pulse shapes and its time derivative for the first pair of excitation pulses ($\delta = 5\,\mu$m – orange, $\delta = 15\,\mu$m – blue).
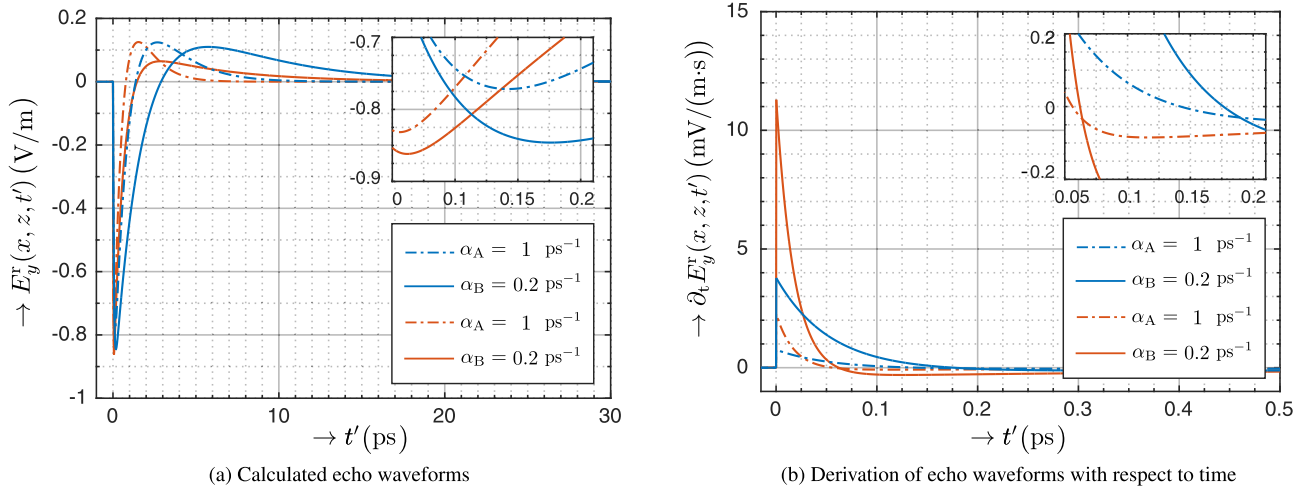

FIGURE 10. Case 2 – Reflected pulse shapes and its time derivative for the second pair of excitation pulses ($\delta = 5\,\mu$m – orange, $\delta = 15\,\mu$m – blue).

the excitation pulse, that is, $c_0/\alpha \gg \delta$. Therefore, the pulse time width of the excitation pulses is to be chosen with respect to this condition.

To find out the influence of β and δ on the desired parameters, we are considering two mutually independent cases. Tables 2 and 3 contain the values of α-coefficients, β and δ. In both cases, the EM constitutive properties of the layer $\epsilon_r = 50$ and $\mu_r = 3$ remain constant.

Based on the parameters shown in Tabs. 2 and 3, the graphical outputs (Figs. 7 to 10) of the obtained echograms $E_y^r(x, z, t'|\alpha_{A,B})$ and its derivative $\partial_t E_y^r(x, z, t'|\alpha_{A,B})$, for both experiments, are below. For the sake of clarity, the zero-crossing regions are zoomed and incorporated in the figures as their insets. From these regions, we can read the key values $t_{r;\alpha_{A,B}}$ and $E_{p;\alpha_{A,B}}$ that are next used to extract the desired material parameters.

TABLE 4. Case 1 – The values of the normalized instants $\bar{t}_{r;\alpha_{A,B}}$ and corresponding peaks $E_{p;\alpha_{A,B}}$ obtained from Fig. 7.

Line type	$\bar{t}_{r;\alpha_{A,B}}$ (−)	$E_{p;\alpha_{A,B}}$ (V/m)
–·–··	$24.108 \cdot 10^{-3}$	-0.8538
——	$12.385 \cdot 10^{-3}$	-0.8618
–·–··	$28.094 \cdot 10^{-3}$	-0.7767
——	$14.407 \cdot 10^{-3}$	-0.7850

It is interesting to observe that in contrast to the incident pulse shapes (see Fig. 5), the reflected ones take both positive and negative values. This fully complies with the enforced cross-layer conditions (see Ref. [15]) and the pertaining EM field equations.

TABLE 5. Case 1 – The values of the normalized instants $\bar{t}_{r;\alpha_{A,B}}$ and corresponding peaks $E_{p;\alpha_{A,B}}$ obtained from Fig. 8.

Line type	$\bar{t}_{r;\alpha_{A,B}}\ (-)$	$E_{p;\alpha_{A,B}}\ (V/m)$
– · – · ·	$102.1 \cdot 10^{-3}$	-0.7994
——	$24.108 \cdot 10^{-3}$	-0.8538
– · – · ·	$120.3 \cdot 10^{-3}$	-0.7202
——	$28.094 \cdot 10^{-3}$	-0.7767

TABLE 6. Case 2 – The values of the normalized instants $\bar{t}_{r;\alpha_{A,B}}$ and corresponding peaks $E_{p;\alpha_{A,B}}$ obtained from Fig. 9.

Line type	$\bar{t}_{r;\alpha_{A,B}}\ (-)$	$E_{p;\alpha_{A,B}}\ (V/m)$
– · – · ·	$35.25 \cdot 10^{-3}$	-0.8461
——	$18.35 \cdot 10^{-3}$	-0.8578
– · – · ·	$12.386 \cdot 10^{-3}$	-0.8618
——	$6.296 \cdot 10^{-3}$	-0.8660

TABLE 7. Case 2 – The values of the normalized instants $\bar{t}_{r;\alpha_{A,B}}$ and corresponding peaks $E_{p;\alpha_{A,B}}$ obtained from Fig. 10.

Line type	$\bar{t}_{r;\alpha_{A,B}}\ (-)$	$E_{p;\alpha_{A,B}}\ (V/m)$
– · – · ·	$142.16 \cdot 10^{-3}$	-0.7717
——	$35.25 \cdot 10^{-3}$	-0.8461
– · – · ·	$56.09 \cdot 10^{-3}$	-0.8316
——	$12.386 \cdot 10^{-3}$	-0.8618

Tables 4 to 7 summarise the instants $t_{r;\alpha_{A,B}}$, normalized to the value of pulse time width $t_{w;\alpha_{A,B}}$, and corresponding peaks $E_{p;\alpha_{A,B}}$ for both cases. It is seen from Eq. (2) that if $\Psi = \Omega$, the reflected field response is identically zero and the metasurface is thus electromagnetically transparent. Equivalently, this condition can be written as

$$Y_0 \cos(\beta_0) = \sqrt{\epsilon_0 \epsilon_r / \mu_0 \mu_r} \qquad (14)$$

where β_0 is the angle of incidence at which the metasurface behaves as transparent. For the considered TE-polarized EM wave, the Eq. (14) can be satisfied when $\mu_r \geq \epsilon_r$. Figure 6 illustrates the angles β_0 satisfying Eq. (14) for three different values $\mu_r = \{75; 100; 150\}$ and constant $\epsilon_r = 50$.

Apparently, in this circumstance, the analytical TDR approach fails, which calls for an alternative approach. It will be next demonstrated that a stochastic optimization approach helps to bypass the limitation.

B. GLOBAL OPTIMIZATION APPROACH

The properties of the problem as defined in Sec. II are set as follows (if not stated otherwise). The feasible decision space Γ is limited by: $1.0 \leq \epsilon_r \leq 100.0$ and $1.0 \leq \mu_r \leq 10.0$. The metasurface thickness is $\delta = 10.0\,\mu m$. The EM fields are excited by a plane wave pulse impinging the metasurface at
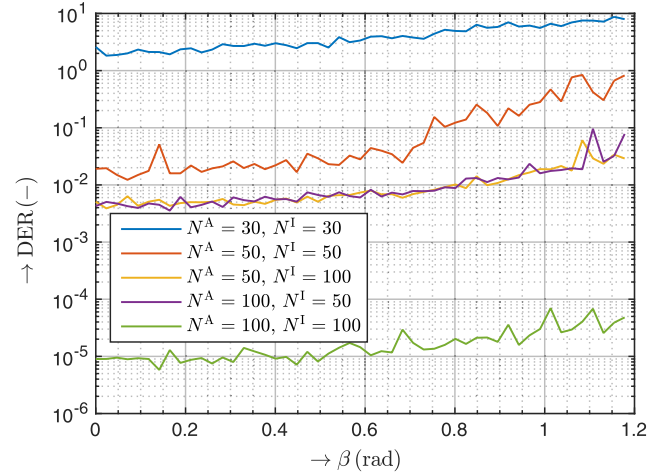
FIGURE 11. Accuracy of the global optimization characterization (average of DER metric from 100 independent runs) for changing incidence angle β and for different number of agents N^A and iterations N^I of PSO algorithm.
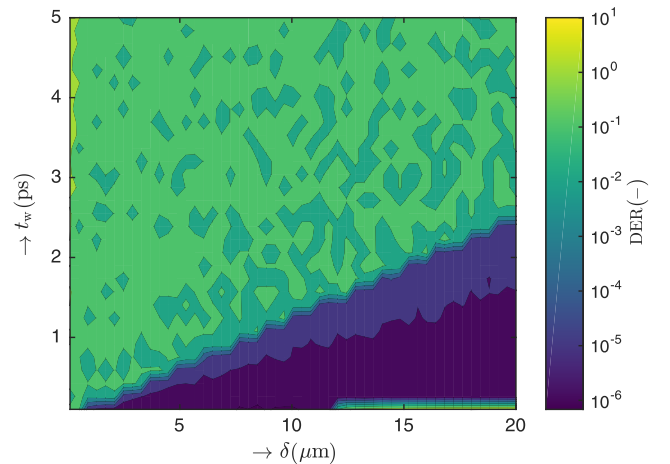
FIGURE 12. Parametric analysis of the average value of DER metric for combinations of metasurface thickness δ and excitation pulse width t_w using PSO algorithm with $N^A = 100$, $N^I = 100$.

angle $\beta = \pi/4\,\mathrm{rad}$. The pulse width is $t_w = 10.0\,\mathrm{ps}$. The time window of observation is given by $0 \leq t \leq 8h/c_0$, where h is the distance from the sheet to the observation point defined as $h = 1.0\,\mathrm{mm}$. The total number of time samples is $N = 101$, which leads to the computational time of $0.1\,\mathrm{ms}$ to evaluate a single electric field response.

All the results of the global optimization algorithm PSO are expressed in the form of decision space error (DER) metric. The latter is generally defined as:

$$\mathrm{DER} = \left[\sum_{d=1}^{D} (u_d - u_d^{\mathrm{true}})^2 \right]^{1/2} \qquad (15)$$

where D is the dimension of the decision space vector $\boldsymbol{u}$ ($D = 2$ in our case). The superscript true denotes the searched (optimal) values: $u_1^{\mathrm{true}} = \epsilon_r = 50.0$, and $u_2^{\mathrm{true}} = \mu_r = 3.0$ in our case.

First, we show the influence of the incidence angle β on the accuracy of the proposed characterization method. The
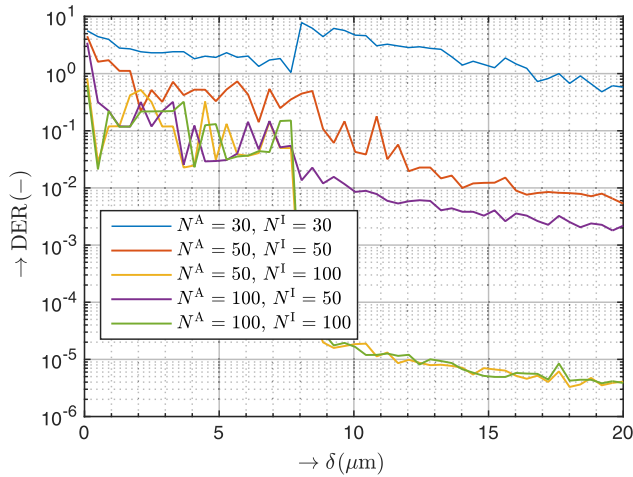
FIGURE 13. Influence of the metasurface thickness δ on accuracy of the global optimization characterization (average of DER metric from 100 independent runs) for different number of agents N^A and iterations N^I of PSO algorithm.
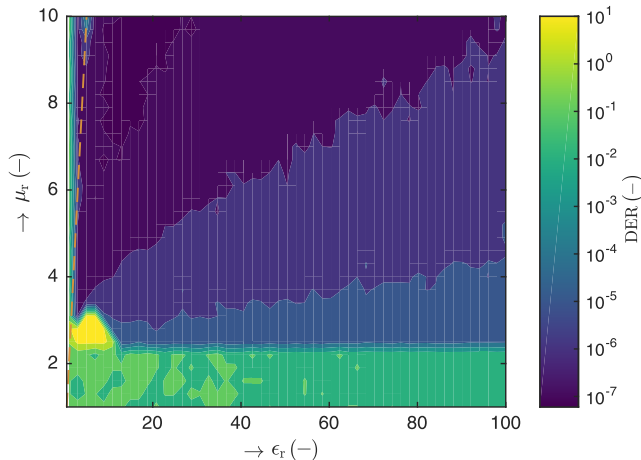

FIGURE 14. Parametric analysis of the average value of DER metric for combinations of metasurface parameters ϵ_r and μ_r using PSO algorithm with $N^A = 100$, and $N^I = 100$.

DER values for different values of β from range $0 \le \beta \le 3\pi/8$ are plotted in Fig. 11. The accuracy slightly decreases with increasing β. The figure compares the accuracy of the method for different number of objective function evaluations (OFE) determined by number of agents and iterations: OFE $= N^A \times N^I$. While for $N^A = N^I = 30$ we get the result with an unacceptable error of order 10^1, all other combinations provide results with DER < 1.0. It is interesting, that curves for combinations $N^A = 50$, $N^I = 100$ and $N^A = 100$, $N^I = 50$ almost overlap. This implies that it does not matter whether we invest the available OFE rather to more agents or iterations.

Next, we investigate how the DER metric depends on the metasurface thickness δ. This knowledge can be of great importance as the parameters of the characterization method (namely the width t_w of the EM wave pulse) can be adjusted according to the thickness of the sample under test. Figure 13 shows the DER metric against values δ from

interval $0.1 \le \delta \le 20.0$ (in μm). Overall, the accuracy of the characterization gets better with growing δ. This effect can be explained by the variable shape of the objective function that depends on the mutual relation between the layer's EM constitutive parameters and its thickness. There is an obvious discontinuity in DER for all combinations of the number of agents and iterations near value $\delta \approx 8.0 \, \mu$m. To further investigate the mutual influence of the t_w and δ parameters, we perform the parametric study over them.

The resulting average values of the DER metric for combinations of values t_w and δ are shown in Fig. 12. Please note that the colormap is scaled logarithmically in the figure. The figure clearly shows a slice where the method achieves the error below the order of 10^{-4}.

The major advantage in using the global optimization algorithm approach is that it works reliably for all combinations of the searched relative permittivity and permeability values. This can be evidenced by the results shown in Fig. 14. Here, a contour plot with a logarithmic scale of DER metric values for different combinations of metasurface parameters ϵ_r and μ_r from the whole space Γ is shown. It proves that a reasonably low value of the error (under 10^{-2}) can be achieved for any pair ϵ_r–μ_r and the error falls below 10^{-5} for a significant part of Γ where $\mu_r > 2.5$. The orange dashed line in Fig. 14 denotes the region of transparency, where the metasurface is not visible for the used EM wave [15]. The methodology based on the global optimization, however, yields the correct material parameters even if the condition of transparency is met.

V. CONCLUSION

We have presented analytical TDR and stochastic-optimization approaches to characterizing the constitutive properties of a scalar metasurface directly in the TD. It has been shown that the analytical TDR approach allows to obtain the material properties exactly in a computationally effortless manner. On the other hand, the analytical methodology fails in the region of TD EM transparency. In this circumstance, the stochastic optimization approach lends itself to remedy the issue. This has been demonstrated on a number of illustrative numerical examples demonstrating the high accuracy and robustness of the optimization approach.

REFERENCES

[1] S. B. Jones, J. M. Wraith, and D. Or, "Time domain reflectometry measurement principles and applications," *Hydrol. Process.*, vol. 16, no. 1, pp. 141–153, 2002.

[2] M. K. Smail, L. Pichon, M. Olivas, F. Auzanneau, and M. Lambert, "Detection of defects in wiring networks using time domain reflectometry," *IEEE Trans. Magn.*, vol. 46, no. 8, pp. 2998–3001, Aug. 2010.

[3] W. A. van Cappellen, R. V. de Jongh, and L. P. Ligthart, "Potentials of ultra-short-pulse time-domain scattering measurements," *IEEE Antennas Propag. Mag.*, vol. 42, no. 4, pp. 35–45, Aug. 2000.

[4] M. Štumpf, "Radar imaging of impenetrable and penetrable targets from finite-duration pulsed signatures," *IEEE Trans. Antennas Propag.*, vol. 62, no. 6, pp. 3035–3042, Jun. 2014.

[5] Y. Koyamada, Y. Sakairi, N. Takeuchi, and S. Adachi, "Novel technique to improve spatial resolution in Brillouin optical time-domain reflectometry," *IEEE Photon. Technol. Lett.*, vol. 19, no. 23, pp. 1910–1912, Dec. 1, 2007.

[6] Y. Huang, J. Luo, M. Pu, Y. Guo, Z. Zhao, X. Ma, X. Li, and X. Luo, "Catenary electromagnetics for ultra-broadband lightweight absorbers and large-scale flat antennas," *Adv. Sci.*, vol. 6, no. 7, Apr. 2019, Art. no. 1801691.

[7] E. Bayati, R. Pestourie, S. Colburn, Z. Lin, S. G. Johnson, and A. Majumdar, "Inverse designed metalenses with extended depth of focus," *ACS Photon.*, vol. 7, no. 4, pp. 873–878, Apr. 2020.

[8] A. Li, S. Singh, and D. Sievenpiper, "Metasurfaces and their applications," *Nanophotonics*, vol. 7, no. 6, pp. 989–1011, Jun. 2018.

[9] A. Epstein and G. V. Eleftheriades, "Huygens' metasurfaces via the equivalence principle: Design and applications," *J. Opt. Soc. Amer. B, Opt. Phys.*, vol. 33, no. 2, pp. A31–A50, 2016.

[10] Y. Vahabzadeh, N. Chamanara, and C. Caloz, "Generalized sheet transition condition FDTD simulation of metasurface," *IEEE Trans. Antennas Propag.*, vol. 66, no. 1, pp. 271–280, Jan. 2018.

[11] S. A. Stewart, T. J. Smy, and S. Gupta, "Finite-difference time-domain modeling of space–time-modulated metasurfaces," *IEEE Trans. Antennas Propag.*, vol. 66, no. 1, pp. 281–292, Jan. 2018.

[12] S. A. Stewart, S. Moslemi-Tabrizi, T. J. Smy, and S. Gupta, "Scattering field solutions of metasurfaces based on the boundary element method for interconnected regions in 2-D," *IEEE Trans. Antennas Propag.*, vol. 67, no. 12, pp. 7487–7495, Dec. 2019.

[13] M. Štumpf, "Pulsed electromagnetic scattering by metasurfaces—A numerical solution based on the Cagniard–DeHoop method of moments," *IEEE Trans. Antennas Propag.*, vol. 69, no. 11, pp. 7761–7770, Nov. 2021.

[14] E. F. Kuester, M. A. Mohamed, M. Piket-May, and C. L. Holloway, "Averaged transition conditions for electromagnetic fields at a metafilm," *IEEE Trans. Antennas Propag.*, vol. 51, no. 10, pp. 2641–2651, Oct. 2003.

[15] M. Štumpf, "Time-domain modeling of thin high-contrast layers with combined dielectric and magnetic properties," *IEEE Antennas Wireless Propag. Lett.*, vol. 19, no. 6, pp. 969–971, Jun. 2020.

[16] T. Brown, C. Narendra, Y. Vahabzadeh, C. Caloz, and P. Mojabi, "On the use of electromagnetic inversion for metasurface design," *IEEE Trans. Antennas Propag.*, vol. 68, no. 3, pp. 1812–1824, Mar. 2020.

[17] T. J. Smy, S. A. Stewart, and S. Gupta, "Surface susceptibility synthesis of metasurface holograms for creating electromagnetic illusions," *IEEE Access*, vol. 8, pp. 93408–93425, 2020.

[18] T. J. Smy and S. Gupta, "Surface susceptibility synthesis of metasurface skins/holograms for electromagnetic camouflage/illusions," *IEEE Access*, vol. 8, pp. 226866–226886, 2020.

[19] N. Engheta, "Metamaterials with high degrees of freedom: Space, time, and more," *Nanophotonics*, vol. 10, no. 1, pp. 639–642, Oct. 2020.

[20] C. Caloz and Z.-L. Deck-Leger, "Spacetime metamaterials—Part I: General concepts," *IEEE Trans. Antennas Propag.*, vol. 68, no. 3, pp. 1569–1582, Mar. 2020.

[21] W. Chew, *Waves and Fields in Inhomogenous Media*. New York, NY, USA: IEEE Press, 1995, chs. 8–9.

[22] A. T. de Hoop and I. E. Lager, "Transient waves along electrical transmission lines. Waves in (1+1)-spacetime," in *Proc. 13th Eur. Conf. Antennas Propag.*, Kraków, Poland, 2019, pp. 1–5.

[23] P. Kadlec, M. Štumpf, and T. Doležal, "Reconstructing the material properties of a scalar metasurface—A stochastic optimization approach," in *Proc. Asia–Pacific Int. Symp. Electromagn. Compat. (APEMC)*, Sep. 2021, pp. 1–4.

[24] J. Robinson and Y. Rahmat-Samii, "Particle swarm optimization in electromagnetics," *IEEE Trans. Antennas Propag.*, vol. 52, no. 2, pp. 397–407, Feb. 2004.

[25] J. M. Johnson and V. Rahmat-Samii, "Genetic algorithms in engineering electromagnetics," *IEEE Antennas Propag. Mag.*, vol. 39, no. 4, pp. 7–21, Aug. 1997.

[26] K. Price, R. M. Storn, and J. A. Lampinen, *Differential Evolution: A Practical Approach to Global Optimization*. Springer, 2006.

[27] S. Karimkashi and A. A. Kishk, "Invasive weed optimization and its features in electromagnetics," *IEEE Trans. Antennas Propag.*, vol. 58, no. 4, pp. 1269–1278, Apr. 2010.

[28] N. Hansen, S. D. Müller, and P. Koumoutsakos, "Reducing the time complexity of the derandomized evolution strategy with covariance matrix adaptation (CMA-ES)," *Evol. Comput.*, vol. 11, no. 1, pp. 1–18, Mar. 2003.

[29] M. Marek, P. Kadlec, and M. Čapek, "FOPS: A new framework for the optimization with variable number of dimensions," *Int. J. RF Microw. Comput.-Aided Eng.*, vol. 30, no. 9, Sep. 2020, Art. no. e22335.

TOMÁŠ DOLEŽAL (Student Member, IEEE) received the M.Sc. degree in electronics and communication, in 2019. He is currently pursuing the Ph.D. degree with the Department of Radio Electronics, Brno University of Technology. His current research interests include modeling and interpretation of electromagnetic waveforms.

PETR KADLEC (Member, IEEE) received the B.Sc., M.Sc., and Ph.D. degrees in electrical engineering from the Brno University of Technology (BUT), Brno, Czech Republic, in 2007, 2009, and 2012, respectively. He is currently a Researcher with the SIX Research Center, BUT. His research interests include global optimization methods and computational methods in electromagnetics.

MARTIN ŠTUMPF (Senior Member, IEEE) received the Ph.D. degree in electrical engineering from the Brno University of Technology (BUT), Brno, Czech Republic, in 2011. After his Ph.D. research, he spent a year and a half as a Postdoctoral Fellow with the ESAT-TELEMIC Division, Katholieke Universiteit Leuven, Leuven, Belgium. He is currently an Associate Professor with the Department of Radioelectronics, BUT. During a three-month period, in 2018, he was a Visiting Professor with the UAq EMC Laboratory, University of L'Aquila, Italy. He has authored the books "*Electromagnetic Reciprocity in Antenna Theory*" (Wiley–IEEE Press, 2017), "*Pulsed EM Field Computation in Planar Circuits: The Contour Integral Method*" (CRC Press, 2018), and "*Time-Domain Electromagnetic Reciprocity in Antenna Modeling*" (Wiley–IEEE Press, 2019). His research interests include modeling of electromagnetic wave phenomena with an emphasis on EMC and antenna engineering.

○ ○ ○